ADVANCED MATERIALS
www.advmat.de

Check for updates

Electrostatic Force–Driven Oxide Heteroepitaxy for Interface Control

Zhaohui Ren, Mengjiao Wu, Xing Chen, Wei Li, Ming Li, Fang Wang, He Tian, Junze Chen, Yanwu Xie, Jiangquan Mai, Xiang Li, Xinhui Lu, Yunhao Lu, Hua Zhang, Gustaaf Van Tendeloo, Ze Zhang, and Gaorong Han**

Oxide heterostructure interfaces create a platform to induce intriguing electric and magnetic functionalities for possible future devices. A general approach to control growth and interface structure of oxide heterostructures will offer a great opportunity for understanding and manipulating the functionalities. Here, it is reported that an electrostatic force, originating from a polar ferroelectric surface, can be used to drive oxide heteroepitaxy, giving rise to an atomically sharp and coherent interface by using a low-temperature solution method. These heterostructures adopt a fascinating selective growth, and show a saturation thickness and the reconstructed interface with concentrated charges accumulation. The ferroelectric polarization screening, developing from a solid–liquid interface to the heterostructure interface, is decisive for the specific growth. At the interface, a charge transfer and accumulation take place for electrical compensation. The facile approach presented here can be extremely useful for controlling oxide heteroepitaxy and producing intriguing interface functionality via electrostatic engineering.

In the past decade, advances in fabrication technology have allowed one to control atomic-level deposition of oxide heterostructures, which results in generating a 2D electron gas,[1] superconductivity,[2–4] ferromagnetism,[3,4] improper ferroelectricity,[5] and vortex electric polarization.[6,7] The rich behavior at the heterostructure interfaces are driven by various forms of symmetry-breaking patterns arising from the complex interactions between their charge, spin, and orbital degrees of freedom.[2,8] Understanding and tailoring these oxide interfaces and functionalities are necessary before considering possible applications, where a design strategy and a rapidly improving expertise are highly desired.[9,10] Classical growth techniques, such as molecular beam epitaxy (MBE) and pulsed laser deposition (PLD), are able to produce oxide interfaces with atomic-level precision, where the selective species are physically deposited on a substrate at a relatively high temperature. Nevertheless, a change in the physical deposition by using an alternative driving force for growth of the oxide heterostructures may create interface differences in structures and properties. van der Waals forces, hydrogen bonding, and electrostatic forces have been shown to drive self-assembly of organically passivated nanoparticles into various structures and films.[11] Numerous van der Waals heterostructures of layered crystals such as graphene, MoS_2, and $MoSe_2$ have been fabricated in this way.[12,13] For complex oxide heterostructures, however, the van der Waals force is too weak to induce epitaxial growth for obtaining a high-quality interface with the formation of strong ionic or covalent bonds. As a comparison, an

Dr. Z. H. Ren, M. J. Wu, W. Li, M. Li, F. Wang, Dr. H. Tian, Dr. X. Li, Dr. Y. H. Lu, Prof. G. R. Han
State Key Laboratory of Silicon Materials
School of Materials Science and Engineering
Cyrus Tang Center for Sensor Materials and Application
Zhejiang University
Hangzhou 310027, China
E-mail: hetian@zju.edu.cn; hgr@zju.edu.cn

X. Chen, Dr. H. Tian, Prof. Z. Zhang
Center of Electron Microscope
School of Materials Science and Engineering
Zhejiang University
Hangzhou 310027, China

Dr. J. Z. Chen, Prof. H. Zhang
School of Materials Science and Engineering
Nanyang Technological University
Block N4.1, 50 Nanyang Avenue, Singapore 639798, Singapore

Prof. Y. W. Xie
Department of Physics
Zhejiang University
Hangzhou 310027, China

Dr. J. Q. Mai, Prof. X. H. Lu
Department of Physics
Chinese University of Hong Kong
Hong Kong 999077, China

Prof. G. Van Tendeloo
EMAT
University of Antwerp
B-2020 Antwerp, Belgium

Prof. G. Van Tendeloo
Nanostructure Research Center
Wuhan University of Technology
430074 Wuhan, China

DOI: 10.1002/adma.201707017

© 2018 WILEY-VCH Verlag GmbH & Co. KGaA, Weinheim

electrostatic force, because of its long-distance interaction, has the ability to significantly change the crystal growth behavior and the resulting morphology.[14] A prominent example is a single-crystal ZnO nanoring formed by a specific epitaxial self-coiling of a nanobelt, originating from the electrostatic attraction between positive Zn^{2+} and negative O^{2-} charged polar surfaces during a solid–vapor process.[15] Actually, an intrinsic polar or polarization character is often involved in complex oxide heterostructures.[1–9] Here we propose that an electrostatic force, originating from a polar surface, can be employed to drive the epitaxial growth of oxide heterostructures, giving rise to the fascinating interface structures and phenomena.

For typical semiconductors, such as ZnO nanobelts[15] and CdTe quantum rods,[16] the polarization surface charge density has been determined to be low as 5.7 and 0.19 μC cm^{-2}, respectively. To demonstrate an electrostatic effect on oxide heteroepitaxy, we chose perovskite ferroelectric materials as a substrate because of their high spontaneous polarization of several tens μC cm^{-2}.[17] In our experiments (see the Experimental Section for detailed information), freestanding $PbTiO_3$ (PTO) nanoplates were selected as a substrate to investigate the polarization-mediated epitaxial growth of functional oxides. In our previous work, these substrates have been characterized to be single crystal and single domain with positive or negative polar {001} facets and an atomically smooth surface (Figure S1, Supporting Information).[18] Very importantly, the PTO nanoplates still maintain a large spontaneous polarization ($P_s \approx 67$ μC cm^{-2}) at room temperature (Figure S2, Supporting Information), close to that of bulk PTO (≈75 μC cm^{-2}). Three typical materials were selected to grow on the ferroelectric PTO substrates to explore the interface: anatase TiO_2, cubic perovskite $SrTiO_3$ (STO) and rhombohedral perovskite $BiFeO_3$ (BFO) (**Figure 1**a–c). The TiO_2/PTO, STO/PTO, and BFO/PTO heterostructures were synthesized by a low-temperature hydrothermal method (100–200 °C, 5 min to 24 h).

As-synthesized powder samples were characterized by grazing-incidence wide-angle X-ray scattering (GIWAXS; Figure S3, Supporting Information) to be pure anatase TiO_2, cubic perovskite STO, and rhombohedral perovskite BFO in addition to tetragonal perovskite PTO. SEM images of the three systems show that continuous and smooth films are formed on the PTO nanoplates (Figure S4A–C, Supporting Information), demonstrating a selective growth on particular polar surface of PTO (Figure S4D–F, Supporting Information). Remarkably, there exists a saturation thickness of the films: ≈13 nm for anatase TiO_2, ≈22 nm for STO, and ≈18 nm for BFO. When such thickness is achieved, an enhanced reactant concentration and prolonged reaction time cannot basically lead to a further growth of the films (Figure S5, Supporting Information). High-angle annular dark-field scanning transmission electron microscopy (HAADF-STEM) (**Figure 2**) shows that the resulting films have a coherent interface with the PTO substrate (indicated by a black arrow). Well-defined and atomically sharp interfaces of TiO_2/PTO, STO/PTO, and BFO/PTO can be observed in Figure 2a–c. From this figure the epitaxial relationship for TiO_2/PTO, STO/PTO, and BFO/PTO can be identified as $\{100\}_t//\{100\}_p$, $\{100\}_s//\{100\}_p$, and $\{100\}_b//\{100\}_p$, respectively, where t, p, s, and b represent TiO_2, $PbTiO_3$, $SrTiO_3$, and $BiFeO_3$, respectively, in perfect agreement with the expectations from Figure 1a–c. Detailed profile intensity measurements (Figure 2d–f) on the lattice spacing across the three interfaces provide evidence for a sharp interface for TiO_2/PTO, STO/PTO, and BFO/PTO. From the displacement of the Ti atoms, we can unambiguously conclude that the TiO_2 and STO films grow on the positive polar surface of the PTO nanoplates,[21] whereas BFO films grow on the negative side since the polarization direction of PTO is opposite to the shift direction of the Ti cation (Figure S2, Supporting Information).

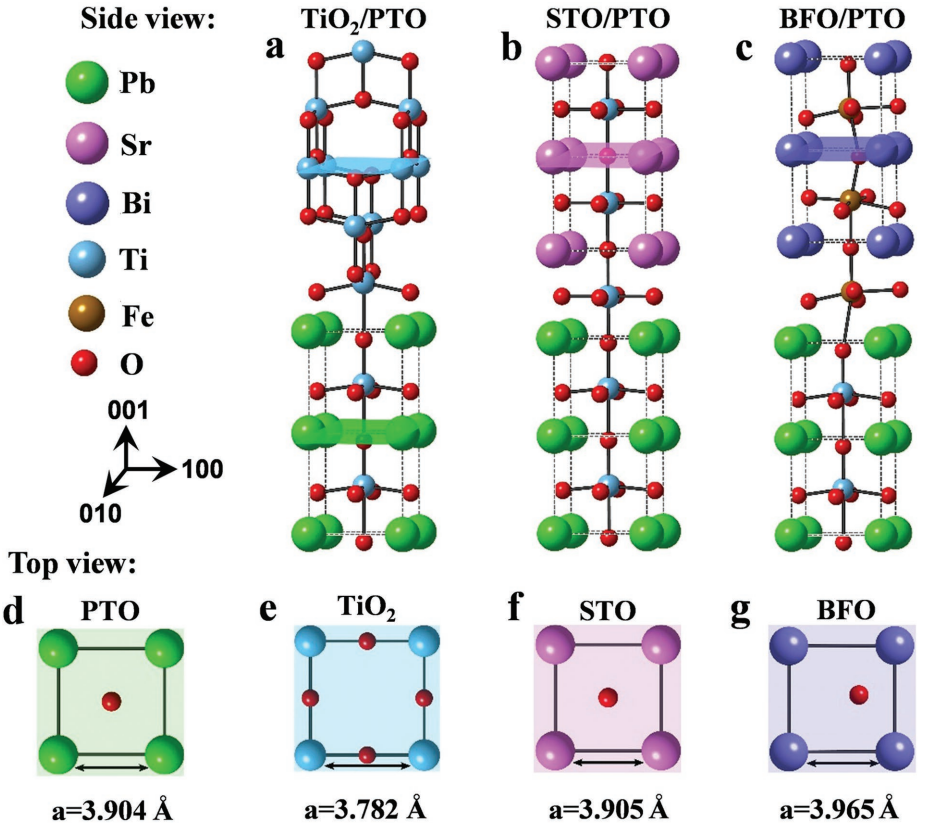

Figure 1. Design of the interface of TiO_2, STO, and BFO on a PTO polar surface. a–c) Structural matching of the TiO_2/PTO, STO/PTO, and BFO/PTO heterostructures from a side view. d–g) Top view of the PTO, TiO_2, STO, and BFO epitaxial growth plane in the structure matching model. The lattice mismatch (δ) is ≈−3.13% (tensile strain) between PTO {100} (3.904 Å)[7] and anatase TiO_2 {100} (3.782 Å),[19] ≈ 0.03% between PTO {100} and STO {100} (3.905 Å),[7] and ≈1.56% (compressive strain) between BFO pseudo-cubic {100} (3.965 Å)[20] and PTO {100}.

© 2018 WILEY-VCH Verlag GmbH & Co. KGaA, Weinheim

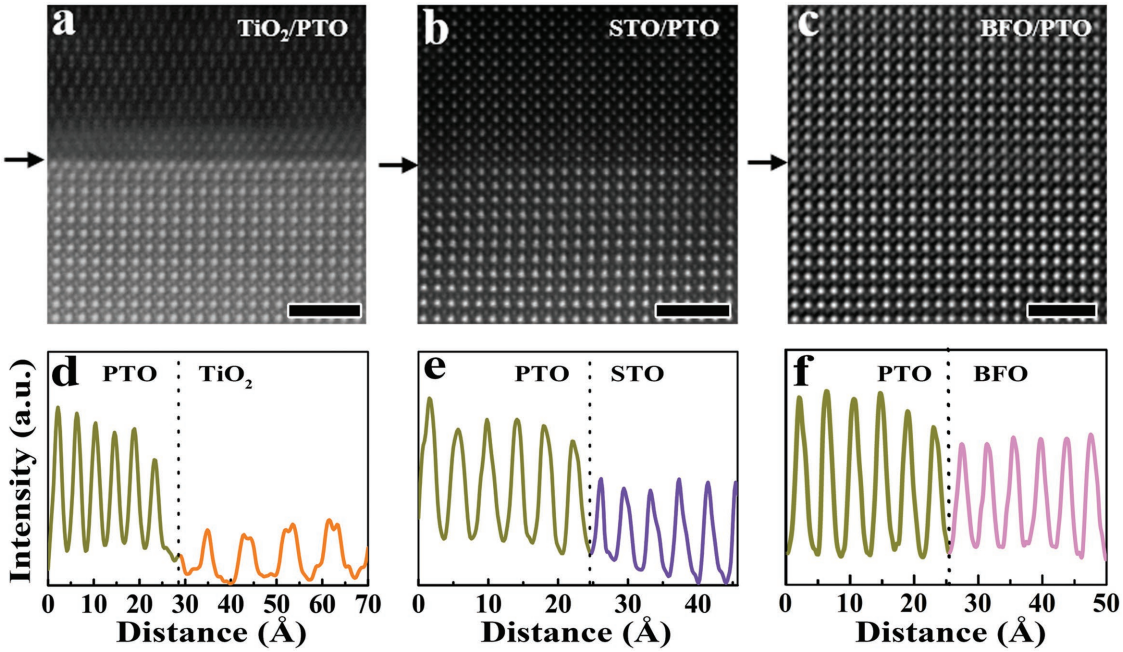

Figure 2. Atomic-level cross-section HAADF-STEM images of a) TiO_2/PTO, b) STO/PTO, and c) BFO/PTO interfaces. The black arrow in each image points to the interface layer; the intensity profiles of the HAADF-STEM images perpendicular to the interface are shown in (d)–(f). Scale bar, 2 nm.

Different from MBE or PLD methods, the selective growth and saturation thickness of the heterostructures should be tightly related to the polar surface of the single-domain PTO nanoplate. The electrostatic effect arising from the ferroelectric polar surface not only drives a specific growth of the heterostructures but also induces a fascinating interface. A distinct atomic reconstruction of PTO has been found at the TiO_2/PTO interface, accompanied by a reconstruction of two layers of anatase TiO_2 near the interface in Figure 2a. In particular, Pb atoms at the interface move 0.5 unit cell along [100] of the tetragonal perovskite PTO. This reconstruction is supported by the prediction of the behavior of the positive polar surface of PTO when exposed to vacuum in order to maintain its large polarization.[22] No such reconstruction, however, occurs at the interfaces of STO/PTO and BFO/PTO, as shown in Figure 2b,c. We argue that the large crystal structure difference and lattice strain for TiO_2/PTO drive the interface reconstruction since a large lattice mismatch was expected to be ≈ −3.13% in Figure 1, whereas a slight mismatch of ≈0.03% and ≈1.56% could exist at the STO/PTO interface and the BFO/PTO interface, respectively. After the formation of the heterostructures, the PTO nanoplates maintain their single-domain character (Figure 2), implying that the strain arising from the lattice mismatch near the interfaces in three systems did not affect the entire PTO nanoplates to form 90° domains.[23] Therefore, the screening of the positive polar surface at the interface should be realized. At this stage, negative ion absorption from the surroundings is no longer accessible to the interface. Hence, surface reconstruction at the interface can be an alternative approach to stabilize ferroelectric polarization at the TiO_2/PTO interface. The displacement of Ti atoms within the first three PTO unit cells near the interface is very low, but it quickly increases to a high and stable value away from the interface (**Figure 3**d). These observations imply that the ferroelectric polarization of PTO is recovered after three unit cells away from the interface.[24] However, according to theoretical calculations in previous work,[22] the structural reconstruction on the positive polar surface of PTO cannot lead to a lower Ti displacement, which implies that the reconstruction cannot be the only way to realize the polarization screening. One possibility is that electrons transfer and accumulate near the interface to compensate the surface charges of PTO. To provide an experimental evidence, electron energy-loss spectra (EELS) of Ti across the interface of TiO_2/PTO have been analyzed (Figure S6, Supporting Information). It is interesting to find that Ti^{3+}/Ti^{4+} significantly increases (Figure S6C, Supporting Information), indicating that a large amount of Ti^{3+} exists at the interface near the PTO side and thus electrons accumulate at the interface as an electronic screening manner for PTO positive polar surface. Accordingly, the interfacial reconstruction and electron transfer play a synergistic role in screening the positive polar surface of PTO nanoplate.

In the STO/PTO system (Figure 3e), the displacement of Ti atoms within PTO is very low near the interface, suggesting that the ferroelectric polarization is significantly suppressed. After about eight unit cells, the displacement of Ti atoms reaches its stable value and the ferroelectric polarization is recovered. Also, the displacement of Ti in the first unit cell of STO is remarkable, suggesting that the STO layer is polarized near the interface.[25,26] The ionic polarization of STO comes out as a response of the discontinuity of polarization at the interface.[27] This could be reasonably considered as an ionic screening of positive polar surface of PTO.[24] The displacement of Ti atoms near the BFO/PTO interface is reduced within six unit cells, suggesting a suppressed polarization of PTO. One should note that BFO and PTO are both ferroelectric and the polarization (P_s)

© 2018 WILEY-VCH Verlag GmbH & Co. KGaA, Weinheim

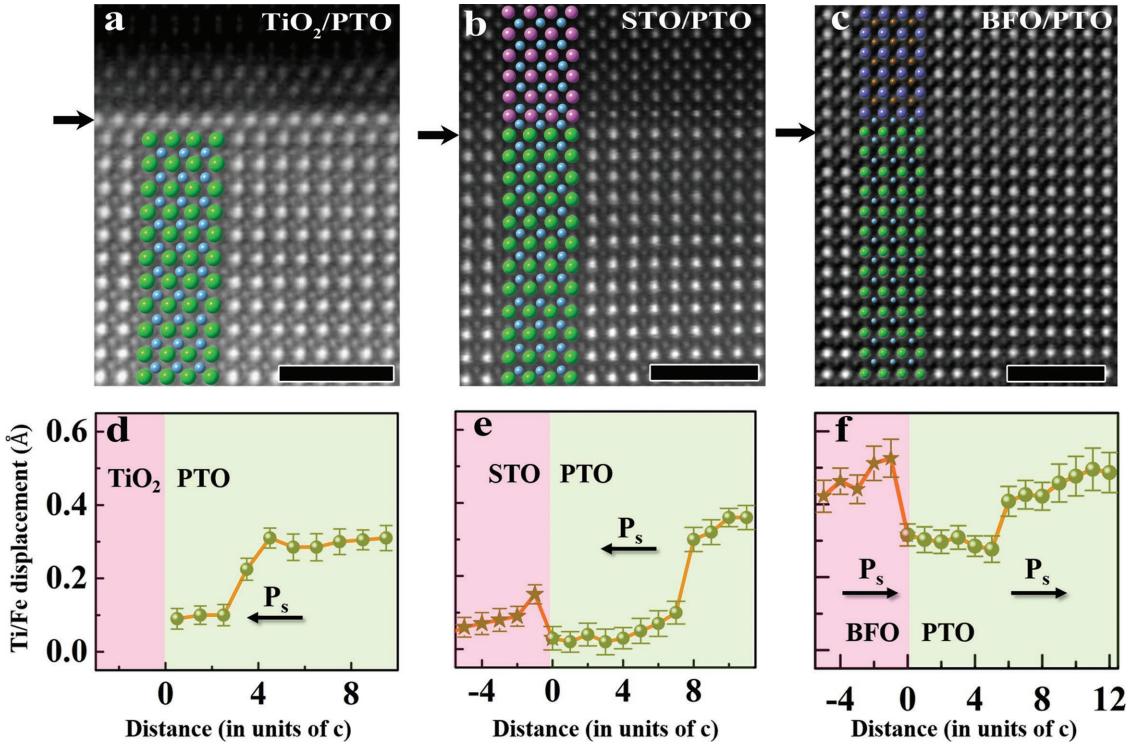

Figure 3. Ti/Fe atom displacements at the TiO_2/PTO, STO/PTO, and BFO/PTO interface region. Atomic-level HAADF-STEM images of the interface region of a) TiO_2/PTO, b) STO/PTO, and c) BFO/PTO, observed along the ⟨100⟩ direction. The Ti atoms (light blue) of PTO and STO are shifted from the center of the Pb atoms (green) or Sr atoms (purple) along the *c*-axis, and the Fe atoms (brown) of BFO shift from the center of the Bi atoms (dark blue). The black arrow in (a) points to the interface layer of the Pb atoms. The average displacements of the Ti/Fe atom shown in (d)–(f) are measured in three unit cells and the distance from the interface is measured in the *c*-axis unit cells. The bars represent the standard deviation of the experimental data. Scale bar, 2 nm.

of a rhombohedral BFO single crystal is ≈35 μC cm^{-2},[28] much lower than that of the PTO nanoplate (≈67 μC cm^{-2}). Different from that of PTO, the displacement of the Fe atoms along the [001] projection is proportional to the BFO polarization along the [111] direction.[29] Moreover, the polarization directions of PTO and BFO are aligned to form a "head-to-tail" configuration in Figure 3f, which is energetically stable.[30] This implies that the spontaneous polarization of BFO could partially screen the polarization of PTO at the negative polar surface.

Above results clearly show that ferroelectric polarization screening at the interfaces in Figure 3 generates novel interfacial structures. However, a complex interface reconstruction or ferroelectric configuration is involved in TiO_2/PTO and BFO/PTO systems. Below the STO/PTO system is further investigated. **Figure 4**a shows an HAADF-STEM image of the cross-section interface of STO/PTO heterostructure; the left color inset presents an atomic-scale EDX map of the interface region, indicating the atomically sharp interface of chemical composition between PTO and STO. To explore the electronic state near the interface, core loss spectra of electron energy-loss spectroscopy were acquired across the interface, as shown in Figure 4b. In both the STO and PTO regions far away from interface, the Ti $L_{2,3}$ edges show a typical four-peak configuration, which is indicative of a Ti^{4+} valence state.[31] In contrast, the two peaks of the Ti L_2 edge merge within three unit cells near the interface. A least-squares fit to Ti^{3+} and Ti^{4+} reference spectra was performed, confirming the coexistence of a high fraction of Ti^{3+} (≈66%) with Ti^{4+} near the interface region. Such value quickly decreases to ≈50% in the next layer on the PTO side. 2D mapping acquired near the interface (right inset of Figure 4a) reveals that Ti^{3+} (yellow) mainly exists within four unit cells on the PTO side, while Ti^{4+} (green) is maintained on the STO side. The existence of Ti^{3+} in PTO side suggests that PTO layer near the interface may be ferroelectric and meanwhile conductive in such STO/PTO system with polarization pointing to the STO side.[32]

In principle, the large amount of Ti^{3+} near the interface would be a result of charge transfer and accumulation. It has been theoretically predicted that the concentrated electrons at the interface can be explained by the existence of oxygen vacancies.[33] To realize a complete polarization screening of PTO, a high charge density of ≈10^{20} cm^{-3} is necessary near the surface.[17] However, such charge density cannot be available from STO layers due to the low charge carrier density (≈10^{14} cm^{-3}) under thermal excitation (hydrothermal temperature of 200 °C, i.e., 473 K) in semiconductor.[34] Hence, it can be reasonable to infer that additional electronic screening should occur within the PTO side. This was supported by the results in Figure 4b, where a large amount of electrons has been identified at the PTO side near the interface other than the STO side, implying that the compensating electrons are provided by PTO nanoplates. To further demonstrate the origin of electrons, STEM-EELS analysis of STO/PTO has been performed (Figure S7, Supporting Information). The O K edge of the PTO side

© 2018 WILEY-VCH Verlag GmbH & Co. KGaA, Weinheim

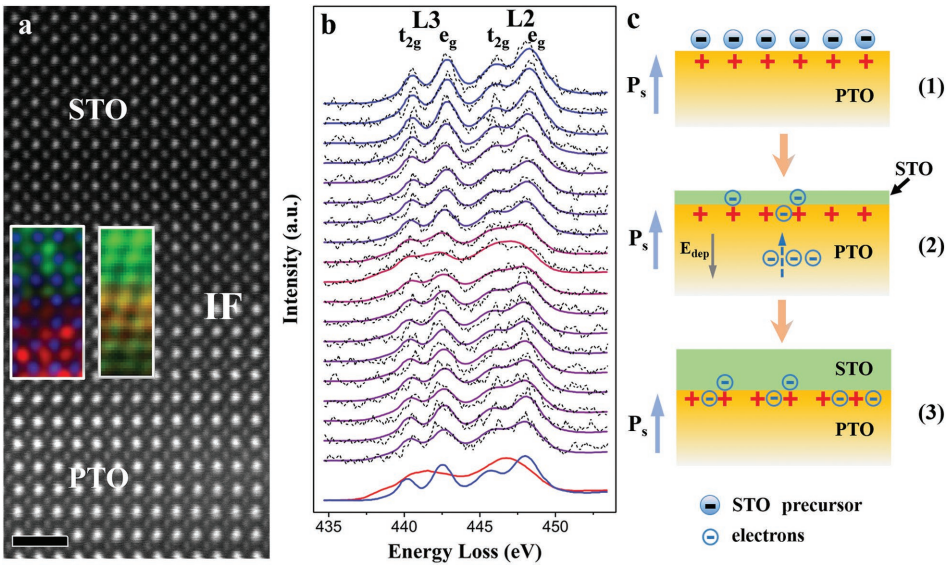

Figure 4. Electron energy-loss spectra across the STO/PTO interface and proposed growth model for STO/PTO heterostructures. The atomic-level cross-section HAADF-STEM image of the STO/PTO heterostructure is shown in (a), where IF represents the interface. The left inset shows the corresponding atomic scale EDX map. Pb, Sr, and Ti correspond to red, green, and blue, respectively. The spatial distribution of Ti^{3+} (yellow) and Ti^{4+} (green) based on EELS analysis is shown in the right side inset. The EELS spectra acquired across the interface are plotted with black dots in (b); the left side of the figure is aligned with the HAADF image. Reference spectra for Ti^{3+} (red) and Ti^{4+} (blue) are shown at the bottom. Colored solid lines show the fit models of each experimental spectrum color-coded by the fractional contribution of Ti^{3+} and Ti^{4+}. c) Schematic illustration of proposed growth model for STO/PTO heterostructures, where (1), (2), and (3) represent the stages (named as steps 1, 2 and 3) in the growth process. The gray arrow in step 2 indicates the depolarizing field E_{dep}, and the light blue dashed arrow indicates the transfer direction of electrons.

(Figure S7B, Supporting Information) indicates that no detectable oxygen deficiency exists at the interface while there are oxygen vacancies in PTO interior away from the interface. Furthermore, an obvious decrease of oxygen atomic percentage has been observed across the entire PTO nanoplate from the interface to negative surface (Figure S7D, Supporting Information). These results indicate that oxygen vacancies would be the origin of electrons accumulated at the interface. It has been well established that the oxygen vacancies from the missing oxygen can compensate the negative polar surface of PTO, and electron carried by missing oxygen ion can transfer to the positive polar surface of PTO,[35] under the driving force of depolarizing field due to an incomplete screening.[36] While in the STO side, insufficient electrons would transfer and accumulate near the interface due to an electrostatic force, and thus an electric field would be generated between the positive bound charges in PTO and the electrons in STO. Such field would polarize the STO within two or three unit cells near the interface, as shown in Figure 3e. Hence, ionic screening from polarized STO and electronic screening from electrons in PTO itself contribute to the complete screening of positive polar surface of PTO in STO/PTO heterostructure.

In the case of BFO/PTO, the polarization of PTO has been partially screened by the spontaneous polarization of BFO, and extra positive charges are needed to compensate the negative polar surface of PTO. As shown in Figure S8D (Supporting Information), oxygen vacancies have been detected in the side of PTO from the interface to the interior. In particular, the valence change of Ti was not observed in Figure S8B in the Supporting Information. These results allow us to expect that such oxygen vacancies served as additional positive charges to screen the negative polar surface of PTO. Hence, the full screening of negative polar surface of PTO has been realized by the spontaneous polarization of BFO and oxygen vacancies of PTO itself.

As a classic dielectric–ferroelectric model, fascinating flux-closure quadrants and polar vortices have been discovered at the STO/PTO interface, originating from a coupling between a polar discontinuity and strain,[6,7] but valence changes of Ti near the interface have not been observed because of the formation of domain walls within PTO for polarization screening.[37] Compared to MBE or PLD methods (above 500 °C), the growth of our heterostructures was realized hydrothermally at a low temperature (100–200 °C). Hence, the single domain or polarized structure of the substrate can be maintained, allowing to drive specific heteroepitaxial growth and generate intriguing interface phenomena via a ferroelectric polarization screening effect. To discuss this effect, a growth model for the STO/PTO heterostructure on the basis of the screening process is proposed and illustrated in Figure 4c.

The screening is crucial for the polarization stability in ferroelectric materials,[22,24,35,38] significantly affecting the molecular adsorption, metal deposition on them, as well as device performance.[39,40] Without an electrode, the screening for a single domain or polarized system is generally realized by negative ions such as OH^- or O^{2-}, adsorbing on the surface, for compensating the positively polarized surface, and oxygen vacancies for negative polarization.[22,35] We argue that this should be the case of a PTO nanoplate exposed to atmosphere, where the displacement of Ti atoms near the positive polar surface of the pure PTO nanoplates is as large as that of the ones far from the surface and the ferroelectric polarization is well stabilized (Figure S9, Supporting Information). When introduced into a hydrothermal system, the polarization screening of the positive polar surface of the nanoplates can be realized by adsorbing charged reaction species, for example, negatively charged STO precursors (Figure S10, Supporting Information) formed at the primary stage consist of STO nuclei with Ti–OH and Sr–OH species adsorption (Figure 4c, step 1). This is because a chemical bonding between STO and PTO becomes more favorable to generate an energetically stable interface. Once STO begins to form a continuous film on PTO, the established screening in step 1 in Figure 4c will be broken and the screening position

© 2018 WILEY-VCH Verlag GmbH & Co. KGaA, Weinheim

changes from the interface between PTO and solution to the interface between STO and PTO. At this stage, electrons in STO would transfer and accumulate near the interface due to an electrostatic force, and meanwhile equal amount of positive bound charges would be generated on the other surface of the STO film. However, due to the fact that the charge carrier density ($\approx 10^{14}$ cm^{-3}) in STO is much lower than the charge density ($\approx 10^{20}$ cm^{-3}) needed for completely screening, extra electrons originating from oxygen vacancies in PTO interior would be driven by the depolarizing field to transfer to the positive polar surface for screening (step 2). Particularly, the STO side is not energetically stable due to the positive bound charges on the surface of STO thin film, which induces further adsorption of negatively charged STO precursors and a rapid growth process of the STO film from step 2 to step 3. As the polarization of PTO near the interface gradually decreased due to the electronic screening, the electrons needed from STO would reduce, accompanied with less positive bound charges, thus a relatively slower growth rate is expected. When the positive polar surface of PTO near the interface is completely screened, the growth of STO stopped, resulting in a saturation thickness of the STO film and a thermodynamically stable heterostructure (step 3 of Figure 4c). This model gives a reasonable explanation for the selective growth, saturation thickness, and reconstructed interface.

To pursue the growth mechanism, the microstructure of STO/PTO at different hydrothermal intervals was investigated in detail. As shown in Figure S10 (Supporting Information), cubic perovskite STO particles with a spherical morphology were formed after a short time without the introduction of PTO nanoplates (Figure S10B,C, Supporting Information), and the zeta potential of the STO sample was measured to be –24 mV (Figure S10D, Supporting Information). It should be noted that the zeta potential of the BFO precursor was measured to be +7.1 mV, accounting for the selective growth of BFO on negative polar surface of PTO. When the nanoplates were introduced, the negatively charged STO precursors get adsorbed on the positive polar surface of PTO very quickly and develop into regular crystals on the surface of the nanoplates (30 s in Figure S11A in the Supporting Information), before forming a continuous thin film with thicknesses of ≈8 nm (3 min in Figure S11B in the Supporting Information) and ≈11 nm (5 min in Figure S11C in the Supporting Information). After 15 min, the thickness of the film rapidly increases to ≈20 nm (Figure S11D, Supporting Information). With time prolonged, a significantly slower growth rate of the STO film is observed (Figure S11H, Supporting Information), and the thickness of STO reaches ≈22 nm after 2 h and this thickness is maintained even when the time is increased to 24 h (Figure S11F,G, Supporting Information).

Such specific growth is presumably attributed to the fact that the polarization screening is basically approached after 2 h. These observations offer convincing evidence to support the polarization screening–based growth model in Figure 4c. According to such model, a change in ferroelectric polarization intensity of the substrate is able to mediate the growth and the corresponding structure of an object film. To further identify such effect, large-size (10 mm × 10 mm × 0.5 mm) polarized single-crystal PMNT ($Pb(Mg_{1/3}Nb_{2/3})O_3$–$PbTiO_3$) substrates were employed to induce the growth of the STO film. Similar to that of the PTO nanoplates, STO films selectively grow on the positive polar surface of the PMNT substrate, whereas no STO crystals were observed on the negative one (Figure S12, Supporting Information). As expected, the saturation thickness of STO films reduces from ≈22 nm on PTO nanoplates to ≈11.2 nm on PMNT substrates because of a lower polarization (≈38 μC cm^{-2}) compared to that of PTO (≈67 μC cm^{-2}).

In summary, our findings indicate that the electrostatic force originating from a polar surface can be effective to drive epitaxial growth of oxide heterostructures by a solution process, giving rise to atomically sharp interfaces. Ferroelectric polarization screening has been revealed to account for the fascinating growth and structures, accompanied with a charge transfer and accumulation near the interface. A combination of growth strategy and interface design, by choosing materials with different polar or polarization intensity or employing a charge transfer between materials, would pave an alternative way to controllable growth of oxide heterostructures with novel functionalities, such as catalytic, electric, and magnetic properties.

Experimental Section

Materials: PTO nanoplates were prepared according to our previous reported method.[18] TiO_2/PTO heterostructures were synthesized by a hydrothermal method as follows: tetrabutyl titanate was dissolved in alcohol solution as precursor, and hydrofluoric acid was used as crystallographic controlling agent. PTO nanoplates were then added to the solution. The reaction was performed in an autoclave at 180 °C for 5 min to 24 h. STO/PTO heterostructures were synthesized by a hydrothermal method as follows: tetrabutyl titanate and strontiumnitrate were mixed in aqueous solution as a precursor, and sodium hydroxide was used as a crystallographic controlling agent. PTO nanoplates were then added to the solution. The reaction was performed in an autoclave at 200 °C for 10 min to 24 h. BFO/PTO heterostructures were synthesized by a hydrothermal method as follows: bismuth nitrate and ferric nitrate nonahydrate were mixed in aqueous solution as a precursor, and potassium hydroxide was used as a crystallographic controlling agent. PTO nanoplates were then added to the solution. The reaction was performed in an autoclave at 200 °C for 10 min to 12 h.

Characterization: The structure of the samples was investigated by XRD (Cu Kα radiation (λ = 1.54056 Å), Thermo ARL X'TRA powder diffractometer), SEM (Hitachi SU-70), TEM (FEI Tecnai G2 F20 S-TWIN), aberration-corrected HAADF-STEM with EELS (FEI Titan G2 80-200 Chemi STEM and FEI Titan 80-300), and FTIR(Fourier Transform Infrared Spectrometry, NICOLET 830). The GIWAXS characterizations were performed at the 23A SWAXS beamline at the National Synchrotron Radiation Research Center, Hsinchu, Taiwan, using a 10 keV primary beam, 3° incident angle, and C9728DK area detector. Zeta potential measurement was conducted by using Zetasizer Nano-ZS.

Supporting Information

Supporting Information is available from the Wiley Online Library or from the author.

Acknowledgements

Z.H.R., M.J.W., and X.C. contributed equally to this work. This work was financially supported by the National Natural Science Foundation

 © 2018 WILEY-VCH Verlag GmbH & Co. KGaA, Weinheim

of China (Grant Nos. 51232006, 51472218, 11474249, 61574123, 11374009, and 11234011), the National 973 Program of China (Grant No. 2015CB654901), National Young 1000 Talents Program of China, the Fundamental Research Funds for the Central Universities (Grant No. 2017FZA4008), and the 111 Project under Grant No. B16042. J.M. and X.L. gratefully thank the beam time and technical supports provided by 23A SWAXS beamline at NSRRC, Hsinchu.

Conflict of Interest

The authors declare no conflict of interest.

Keywords

electrostatic force, ferroelectric polarization screening, interfaces, oxide heterostructures

Received: November 30, 2017
Revised: July 5, 2018
Published online:

[1] A. Ohtomo, H. Y. Hwang, *Nature* **2004**, *427*, 423.
[2] N. Reyren, S. Thiel, A. D. Caviglia, L. Fitting Kourkoutis, G. Hammerl, C. Richter, C. W. Schneider, T. Kopp, A.-S. Rüetschi, D. Jaccard, M. Gabay, D. A. Muller, J.-M. Triscone, J. Mannhart, *Science* **2007**, *317*, 1196.
[3] L Li, C. Richter, J. Mannhart, R. C. Ashoori, *Nat. Phys.* **2011**, *7*, 762.
[4] J. A. Bert, B. Kalisky, C. Bell, M. Kim, Y. Hikita, H. Y. Hwang, K. A. Moler, *Nat. Phys.* **2011**, *7*, 767.
[5] E. Bousquet, M. Dawber, N. Stucki, C. Lichtensteiger, P. Hermet, S. Gariglio, J.-M Triscone, P. Ghosez, *Nature* **2008**, *452*, 732.
[6] Y. L. Tang, Y. L. Zhu, X. L. Ma, A. Y. Borisevich, A. N. Morozovska, E. A. Eliseev, W. Y. Wang, Y. J. Wang, Y. B. Xu, Z. D. Zhang, S. J. Pennycook, *Science* **2015**, *348*, 547.
[7] A. K. Yadav, C. T. Nelson, S. L. Hsu, Z. Hong, J. D. Clarkson, C. M. Schlepütz, A. R. Damodaran, P. Shafer, E. Arenholz, L. R. Dedon, D. Chen, A. Vishwanath, A. M. Minor, L. Q. Chen, J. F. Scott, L. W. Martin, R. Ramesh, *Nature* **2016**, *530*, 198.
[8] H. Y. Hwang, Y. Iwasa, M. Kawasaki, B. Keimer, N. Nagaosa, Y. Tokura, *Nat. Mater.* **2012**, *11*, 103.
[9] D. Lu, D. J. Baek, S. S. Hong, L. F. Kourkoutis, Y. Hikita, H. Y. Hwang, *Nat. Mater.* **2016**, *15*, 1255.
[10] M. O'Sullivan, J. Hadermann, M. S. Dyer, S. Turner, J. Alaria, T. D. Manning, A. M. Abakumov, J. B. Claridge, M. J. Rosseinsky, *Nat. Chem.* **2016**, *8*, 347.
[11] Z. L. Zhang, S. C. Glotzer, *Nano Lett.* **2004**, *4*, 1407.
[12] A. Koma, *Thin Solid Films* **1992**, *216*, 72.
[13] D. Jariwala, T. J. Marks, M. C. Hersam, *Nat. Mater.* **2016**, *16*, 170.
[14] X. Y. Kong, Y. Ding, R. Yang, Z. L. Wang, *Science* **2004**, *303*, 1348.
[15] X. Y. Kong, Z. L. Wang, *Nano Lett.* **2003**, *3*, 1625.
[16] R. Krishnan, M. A. Hahn, Z. H. Yu, J. Silcox, P. M. Fauchet, T. D. Krauss, *Phys. Rev. Lett.* **2004**, *92*, 216803.
[17] V. M. Fridkin, *Ferroelectric Semiconductors*, Consultants Bureau, New York **1980**.
[18] C. Y. Chao, Z. H. Ren, Y. H. Zhu, Z. Xiao, Z. Y. Liu, G. Xu, J. Q. Mai, X. Li, G. Shen, G. R. Han, *Angew. Chem.* **2012**, *124*, 9417; *Angew. Chem., Int. Ed.* **2012**, *51*, 9283.
[19] J. K. Burdett, T. Hughbanks, G. J. Miller, J. W. Richardson, J. V. Smith, *J. Am. Chem. Soc.* **1987**, *109*, 3639.
[20] F. Kubel, H. Schmid, *Acta Crystallogr. B* **1990**, *46*, 698.
[21] C. L. Jia, V. Nagarajan, J. Q. He, L. Houben, T. Zhao, R. Ramesh, K. Urban, R. Waser, *Nat. Mater.* **2007**, *6*, 64.
[22] K. Garrity, A. Kakekhani, A. Kolpak, S. Ismail-Beigi, *Phys. Rev. B* **2013**, *88*, 045401.
[23] R. W. Cahn, *Adv. Phys.* **1954**, *3*, 363.
[24] M. F. Chisholm, W. D. Luo, M. P. Oxley, S. T. Pantelides, H. N. Lee, *Phys. Rev. Lett.* **2010**, *105*, 197602.
[25] J. B. Neaton, K. M. Rabe, *Appl. Phys. Lett.* **2003**, *82*, 1586.
[26] M. Dawber, C. Lichtensteiger, M. Cantoni, M. Veithen, P. Ghosez, K. Johnston, K. M. Rabe, J.-M. Triscone, *Phys. Rev. Lett.* **2005**, *95*, 177601.
[27] M. Dawber, N. Stucki, C. Lichtensteiger, S. Gariglio, J. M. Trisone, *J. Phys.: Condens. Matter* **2008**, *20*, 264015.
[28] D. Lebeugle, D. Colson, A. Forget, M. Viret, P. Bonville, J. F. Marucco, S. Fusil. *Phys. Rev. B* **2007**, *76*, 024116.
[29] Y. M. Kim, A. Morozovska, E. Eliseev, M. P. Oxley, R. Mishra, S. M. Selbach, T. Grande, S. T. Pantelides, S. V. Kalinin, A. Y. Borisevich, *Nat. Mater.* **2014**, *13*, 1019.
[30] C. L. Jia, S. B. Mi, K. Urban, I. Vrejoiu, M. Alexe, D. Hesse, *Nat. Mater.* **2008**, *7*, 57.
[31] A. Ohtomo, D. A. Muller, J. L. Grazul, H. Y. Hwang, *Nature* **2002**, *419*, 378.
[32] X. H. Liu, J. D. Burton, E. Y. Tsymbal. *Phys. Rev. Lett.* **2016**, *116*, 197602.
[33] N. Pavlenko, T. Kopp, E. Y. Tsymbal, J. Mannhart, G. A. Sawatzky, *Phys. Rev. B* **2012**, *86*, 064431.
[34] I. C. Crawford, *Ferroelectrics* **1970**, *1*, 23.
[35] R. V. Wang, D. D. Fong, F. Jiang, M. J. Highland, P. H. Fuoss, C. Thompson, A. M. Kolpak, J. A. Eastman, S. K. Streiffer, A. M. Rappe, G. B. Stephenson, *Phys. Rev. Lett.* **2009**, *102*, 047601.
[36] M. Y. Zhuravlev, R. F. Sabirianov, S. S. Jaswal, E. Y. Tsymbal, *Phys. Rev. Lett.* **2005**, *94*, 246802.
[37] A. Torres-Pardo, A. Gloter, P. Zubko, N. Jecklin, C. Lichtensteiger, C. Colliex, J.-M. Triscone, O. Stéphan, *Phys. Rev. B* **2011**, *84*, 220102(R).
[38] S. V. Kalinin, D. A. Bonnell, *Phys. Rev. B* **2001**, *63*, 125411.
[39] K. Garrity, A. M. Kolpak, S. Ismail-Beigi, E. I. Altman, *Adv. Mater.* **2010**, *22*, 2969.
[40] L. Sánchez-García, M. O. Ramírez, P. Molina, F. Gallego-Gómez, L. Mateos, E. Yraola, J. J. Carvajal, M. Aguiló, F. Díaz, C. Heras, L. E. Bausá, *Adv. Mater.* **2014**, *26*, 6447.

© 2018 WILEY-VCH Verlag GmbH & Co. KGaA, Weinheim